Journal Pre-proofs

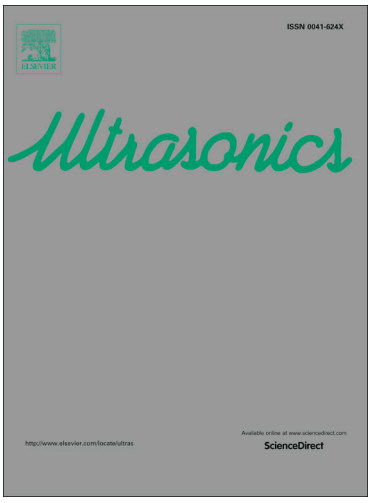

Probing the limits of full-field linear Local Defect Resonance identification for deep defect detection

Joost Segers, Saeid Hedayatrasa, Gaétan Poelman, Wim Van Paepegem, Mathias Kersemans

PII: S0041-624X(20)30069-X
DOI: https://doi.org/10.1016/j.ultras.2020.106130
Reference: ULTRAS 106130

To appear in: *Ultrasonics*

Received Date: 30 September 2019
Revised Date: 4 February 2020
Accepted Date: 6 March 2020

Please cite this article as: J. Segers, S. Hedayatrasa, G. Poelman, W. Van Paepegem, M. Kersemans, Probing the limits of full-field linear Local Defect Resonance identification for deep defect detection, *Ultrasonics* (2020), doi: https://doi.org/10.1016/j.ultras.2020.106130

Probing the limits of full-field linear Local Defect Resonance identification for deep defect detection

Joost Segers[1#], Saeid Hedayatrasa[1,2], Gaétan Poelman[1,2], Wim Van Paepegem[1] and Mathias Kersemans[1]

[1] Mechanics of Materials and Structures (UGent-MMS), Department of Materials, Textiles and Chemical Engineering (MaTCh*)*, Ghent University, Technologiepark-Zwijnaarde 46, 9052 Zwijnaarde, Belgium

[#] Corresponding author, Joost.Segers@ugent.be

[2] SIM Program M3 DETECT-IV, Technologiepark-Zwijnaarde 48, B-9052 Zwijnaarde, Belgium

Abstract

Local Defect Resonance (LDR) is exploited for non-destructive testing (NDT) by using ultrasonic vibrations to get a localized resonant activation of defected zones. The LDR technique relies on the local stiffness difference between the defect and the sound material. Analyzing the structure's displacement field at this localized resonance frequency reveals the defect's location and provides information about the defect's characteristics, i.e. geometry, size and depth.

In this study, the opportunities and limitations of linear LDR for NDT of materials are investigated in a parametric way. Both finite element simulations and experiments (using scanning laser Doppler vibrometry) are performed for aluminum alloy and carbon fiber reinforced polymer coupons with flat bottom holes and delaminations ranging in both depth and diameter. The resonance frequencies as well as the associated defect-to-background ratios are parametrically evaluated.

For shallow defects, a clear LDR is observed caused by the strong local stiffness reduction at the defect. On the contrary, deep defects are associated with a limited stiffness decrease that results in the absence of LDR behavior.

The local stiffness reduction at damages is further exploited using a weighted band power calculation. It is shown that using this technique, deep defects can be detected for which no LDR behavior was observed.

Keywords

Composites, NDT, Local defect resonance, laser Doppler vibrometry, weighted band power

1. Introduction

Composite materials (e.g. carbon fiber reinforced polymer (CFRP)) show high specific strength and stiffness, and are increasingly used in load bearing components. A concern in the use of composites is that the layered material structure is susceptible to internal damages. These damages can be introduced during the manufacturing process as well as during the operational life. Reliable detection of internal damage features by means of non-destructive testing (NDT) is of utmost importance.

In 1993, Tenek et al. [1] investigated the dynamic behavior of locally delaminated composites. At relatively high excitation frequencies (typically ultrasound), the delaminations showed a local resonance providing a high vibrational contrast between the defected and sound areas of the component. This phenomenon was further described by Solodov et al. [2] and is referred to as local

defect resonance (LDR). When the specimen is excited at a LDR frequency the defect can be localized and, to a certain extent, evaluated by measuring the structure's operational deflection shape (ODS). In general, a scanning laser Doppler vibrometer (SLDV) is used to measure the full-field out-of-plane vibrational surface response. Recently, a 3D infrared SLDV has been used by the present authors demonstrating that the concept of LDR can be equally extended toward the in-plane vibrations [3].

Detection of LDRs in operational deflection shapes for defect detection in composites has been shown to be successful for flat bottom holes (FBH) [4-11], inserts [10-13], disbonds [8, 9, 12, 14] and barely visible impact damages (BVID) [3, 10-12, 15-18]. Despite these promising experimental studies, a critical remark has to be made concerning the depth of the investigated damages. All successfully detected defects (described in the references) should be considered 'shallow defects', as they were all located at depths less than half the thickness of the sound material. Considering that the existence of LDR is linked to the difference in stiffness between the defect and the surrounding sound material, it may be expected that a deep defect (that corresponds to a limited local stiffness reduction in the top surface) can be challenging to detect by means of LDR.

In this study, the opportunities and limitations of the linear LDR method for deep defects are investigated through a parametric study. Aluminum and CFRP coupons with FBHs are evaluated by FE simulation and experimentally. Moreover, LDR behavior of FBHs and delaminations of the same depth are compared by FE simulation. The analytically predicted LDR frequency is also included as a benchmark and its validity range is highlighted. The defects' diameter *d* and local material thickness t_{defect} are varied in order to investigate the influence of defect size and depth on the LDR behavior. The local stiffness reduction and hence, the existence of LDR, is related to the relative thickness *k* which is defined as the ratio of defect thickness (t_{defect}) over base material thickness (t_{base}): $k = 100 * \frac{t_{defect}}{t_{base}}$ (%) (see also Figure 1 for definition of t_{defect} and t_{base}). Thus, small *k* values (*k* < 50 %) correspond to shallow defects (i.e. small t_{defect}) while high *k* values (*k* > 50 %) correspond to deep defects (i.e. high t_{defect}).

The first section describes the setup of the finite element simulations and the experimental approach, which are used to study the LDR behavior of the FBHs and delaminations. Next, for both materials, the obtained defects' resonance frequencies as well as the associated defect-to-background ratios are parametrically evaluated in function of defect depth and size. Apart from the classical LDR identification, an approach is presented for defect detection using (weighted) band power calculation. This method is discussed in Section 5. Finally, the conclusions are summarized.

2. Materials and methods

2.1. Finite element simulation

In order to investigate the LDR behavior for a range of defect parameters, an implicit finite element (FE) simulation model is developed (in Abaqus/CAE). The geometrical model parameters are schematically shown in Figure 1. The model consists of a flat 200 mm by 150 mm coupon with one defect of diameter *d* and local thickness t_{defect}. In accordance with the experimental samples, the thicknesses t_{base} are 5 mm and 5.43 mm for the Al and CFRP coupon, respectively. Also, the elastic material properties (Young's modulus *E*, Poisson coefficient *v* and shear modulus *G*) used in the simulation are identical to these of the experimental test specimens (see Table 1). Each of the 24

laminae of the $[(45/0/-45/90)]_{3s}$ CFRP coupon is modelled as an element layer with the material properties listed in Table 1 and local orientation according to the ply angle.

Table 1: Material properties used in FE simulation.

	ρ (kg/m³)	E_1 (GPa)	E_2 (GPa)	E_3 (GPa)	ν_{12} (-)	ν_{13} (-)	ν_{23} (-)	G_{12} (GPa)	G_{13} (GPa)	G_{23} (GPa)
Al-alloy AlMgSi1 [19]	2700	70.00	70.00	70.00	0.34	0.34	0.34	26.12	26.12	26.12
CFRP UD lamina [20]	1528	108.87	9.61	10.04	0.33	0.28	0.49	5.11	5.15	3.29

To reduce the calculation time, the bottom halve of the model is disregarded and symmetric boundary conditions are imposed on the horizontal center line. The remaining top part of the coupon is modelled using a uniform mesh of linear eight node continuous shell elements (type SC8R). In the thickness direction, the model is divide into 24 element layers. In case of a FBH defect, a specific amount of the layers is eliminated at the location of the FBH. In the specific case of a delamination, the defect is modelled using duplicated overlapping nodes (i.e. a seam crack with no interfacial interactions) in between two element layers. The parametric space of the investigated defects is listed in Table 2. The thickness of the defects is changed in steps of 2 elements layers resulting in the $\Delta k = 2/24 = 8.3$ %.

Table 2: Defect characteristics modelled in the FE simulation.

Material	Defect type	*d* (mm)	*k* (%)
Al-alloy	FBH	10, 15, 20, 25, 35	8.3, … (Δk = 8.3) … , 92
CFRP $[(45/0/-45/90)]_{3s}$	FBH	10, 12.5, 15, 20, 25, 30	8.3, … (Δk = 8.3) … , 92
	Delamination	15	8.3, … (Δk = 8.3) … , 92

The natural frequencies and corresponding mode shapes of the system are calculated using the Lanczos solver up to a maximum frequency of 150 kHz. Based on a mesh-convergence study, a mesh size of 1 mm is used in the in-plane directions that corresponds to 17 and 10 elements per wavelength at the highest frequency of interest for the Al and CFRP coupon, respectively. The total model contains around 370,000 mesh elements. No artificial noise was added to the computed mode shapes. Instead, the results and conclusions obtained using the numerical data are validated using experimental measurements.

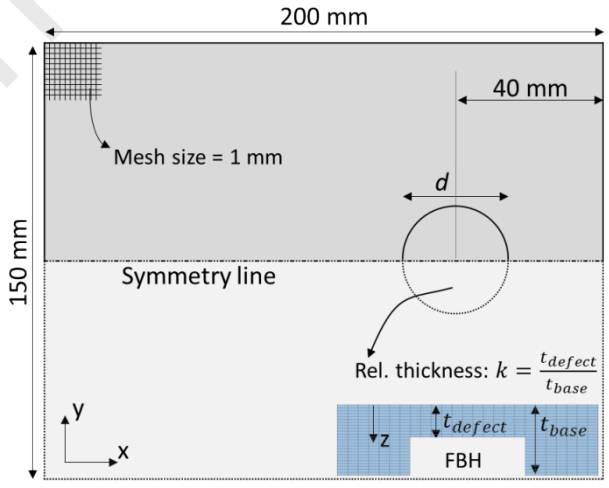

Figure 1: Schematic view of the finite element simulation model.

2.2. SLDV experiment

To assist and validate the numerical computations, several full-field experimental recordings are performed. The broadband vibration response of four flat square plates with multiple FBHs is measured using a 3D infrared scanning laser Doppler vibrometer (SLDV, Polytec PSV-500-3D Xtra). Figure 2 shows the backside for one out of the three Al-alloy (AlMgSi1) coupons and for the CFRP coupon. Their material properties are listed in Table 1. The CFRP plate is manufactured (autoclave) out of 24 unidirectional (UD) carbon fiber laminae according to the quasi-isotropic layup $[(45/0/-45/90)]_{3s}$. The FBH defects are visible and the diameters *d* and relative thicknesses *k* are listed. For each aluminum plate, the FBHs have a fixed diameter but range in thickness. The CFRP plate contains FBHs which range in both diameter and thickness. As listed in Figure 2, the plates contain in total four through holes (i.e. *k* = 0 %) that were introduced for a different study.

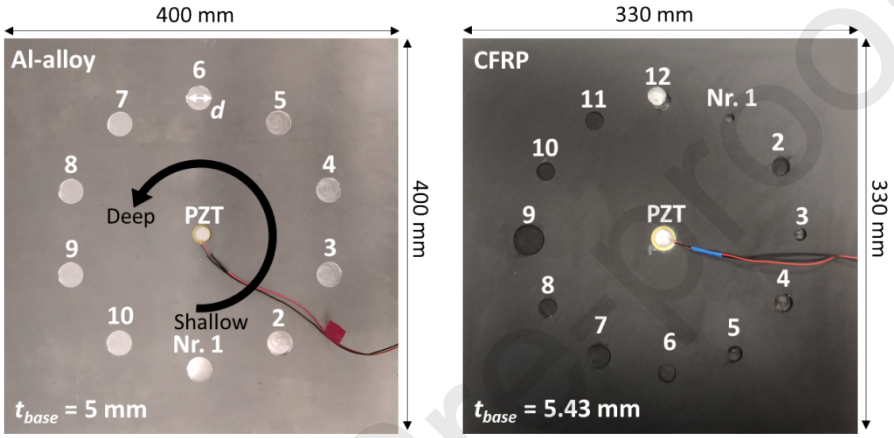

		Nr.	1	2	3	4	5	6	7	8	9	10
Al-alloy	Plate 1	*d* (mm)	15	15	15	15	15	15	15	15	15	15
		k (%)	0	0	12	29	39	49	59	70	76	83
	Plate 2	*d* (mm)	25	25	25	25	25	25	25	25	25	25
		k (%)	0	6	18	27	38	54	59	66	78	87
	Plate 3	*d* (mm)	35	35	35	35	35	35	35	35	35	35
		k (%)	9	13	20	30	43	57	64	71	83	93

	Nr.	1	2	3	4	5	6	7	8	9	10	11	12
CFRP	*d* (mm)	7.0	15.0	10.0	15.0	12.5	15.0	20.0	15.0	25.0	15.0	15.0	15.0
	k (%)	29	20	31	29	30	39	31	49	31	58	67	0

Figure 2: Backside of test specimens with FBHs ranging in relative thickness *k* and diameter *d*.

All coupons are excited using a low power piezoelectric (PZT) patch (type EPZ-20MS64W from Ekulit, with a diameter of 12 mm) bonded to the backside (see Figure 2). The PZT actuator is supplied with a linear burst chirp signal (i.e. linear swept sine followed by a zero signal for 10% of the total signal length). The chirp frequency starts at 1 kHz and ends at 100 kHz for the Al-alloy plates and at 150 kHz for the CFRP plate. The voltage of excitation is amplified 50 times to 150 Vpp (by a Falco System WMA-300 voltage amplifier) to increase the input energy. The in-plane and out-of-plane vibrational response of the flat front side is measured using the 3D SLDV, however, only the out-of-plane velocity component is used in this investigation. For each scan point, 10,000 time samples are recorded with a sampling rate of 250 kS/s (i.e. signal length of 40 ms) and 512 kS/s (i.e. signal length of 20 ms) for the Al-alloy and CRFP plates respectively. Fast Fourier transform (FFT) (after applying a Hanning window) is performed to obtain the ODS at each frequency bin.

This excitation and measurement setup is the most optimal for LDR excitation and detection. Using non-contact excitation methods (e.g. air coupled ultrasound transducers) or a less sensitive velocity measurement device can be more practical but will decrease the LDR detectability performance.

2.3. Identification of LDR frequency

From each FE simulation of a specific defect, a large number of mode shapes is obtained. In order to identify the specific mode shape corresponding to the LDR of the defect, the defect-to-background ratio DBR is calculated as:

$$DBR(f) = \frac{\Omega_{healthy}}{\Omega_{defect}} \frac{\sum_{i=1}^{n_{defect}} V_Z(x_i,y_i,f)}{\sum_{i=1}^{n_{healthy}} V_Z(x_i,y_i,f)} \quad (1)$$

Where Ω_{defect} is the defected area that contains n_{defect} measurement points and $\Omega_{healthy}$ is the surrounding healthy area with $n_{healthy}$ measurement points. $V_Z(x_i,y_i,f)$ is the magnitude of out-of-plane velocity of the point at location (x_i,y_i) for the mode shape corresponding to frequency f. A uniform measurement point grid size of 1.5 mm is used. Thus for each mode shape, the DBR equals the average amplitude of vibration at the defect's location compared to the average amplitude of vibration at the remainder of the coupon. As a result, a local maximum in the *DBR(f)* curve is related to a LDR. A similar procedure is followed to identify the LDR frequency from the experimental measurements. In this case, the DBR is calculated for each ODS and $V_Z(x_i,y_i,f)$ equals the amplitude of out-of-plane velocity of the scan point at location (x_i,y_i) for the ODS at frequency *f*. This LDR identification procedure is further illustrated in Section 3.

Next to the numerical and experimental identification of the LDR frequency, an analytical prediction can be made [4, 5]:

$$LDR_{freq} \approx \frac{6.4\, t_{defect}}{d^2} \sqrt{\frac{E}{12\rho(1-\nu^2)}} \quad (2)$$

According to Eq. 2, it is predicted that the LDR frequency linearly depends on the ratio of defect thickness over diameter squared: $\frac{t_{defect}}{d^2}$. This analytical prediction assumes clamped boundary and thin plate conditions for the resonating defect. These assumptions limit the validity of Eq. 2 to defects with small relative thickness and large diameter-to-thickness ratio: $\frac{d}{t_{defect}} > (7 \text{ to } 10)$ [5] .

3. LDR behavior of FBHs in aluminum plate

For each defect, the vibrational response in frequency domain is analyzed and the LDR frequency (f_{LDR}) is identified. As an example, the experimental identification of the LDR frequency using *DBR(f)* calculation (see also Section 2.3) is illustrated for the FBHs of *k* = 18, 27 and 59 % and *d* = 25 mm in the Al coupon (see Figure 3). For the shallow defect, i.e. FBH with *k* = 18 %, the *DBR(f)* curve shows a clear maximum at the fundamental LDR frequency (14 kHz) of the defect (see ODS in Figure 3 (a)). Other local maxima correspond to higher order LDR modes (see ODS in Figure 3 (b,c)). Note that the ODS at 45 kHz (Figure 3 (c)) by coincidence also shows the higher order LDR mode of another shallow FBH.
For the FBH of *k* = 27 %, a similar observation can be made but with a clear reduction in maximum DBR amplitude. The corresponding ODSs are presented in Figure 3 (d,e). For the deep defect at *k* = 59 %, the DBR curve does not show a clear peak anymore and thus no LDR behavior could be identified (see also inset of Figure 3). In this case, the ODS related to the maximum DBR corresponds rather to a global plate resonance at 8 kHz with an anti-node coinciding with the location of the defect (see Figure 3 (f)).

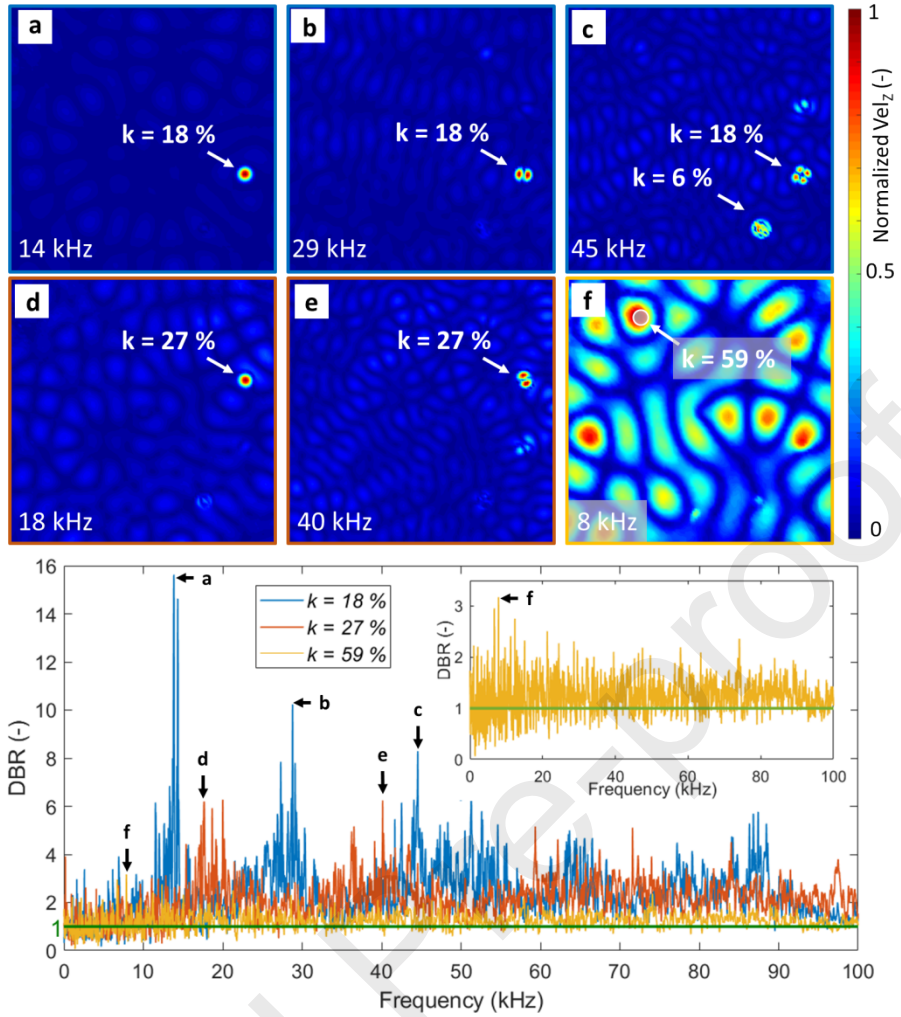

Figure 3: Experimentally obtained defect-to-background ratio (DBR) in function of frequency for three FBHs in the Al-alloy plate (d = 25 mm, k = 18, 27 and 59 %). Several ODS maps at local maxima in the DBR curve are added.

In an identical way, the LDR frequency is identified for all numerical and experimental investigated defects. The results are grouped in Figure 4. Each defect has a specific diameter d and relative thickness k. The data for defects of the same diameter are given the same color (see legend) whereas the k values are shown on the x-axis. Filled markers refer to simulations whereas the empty markers correspond to experimental results. Figure 4 (a) and (b) both show f_{LDR} in function of the defect's relative thickness whereas the DBR value corresponding to f_{LDR} is shown in Figure 4 (c) and (d). The results are separated into small and large diameter defects to improve the readability of the figures. For the FBHs with d = 10, 15 and 20 mm (orange, yellow and purple color, respectively), the analytical prediction of f_{LDR} using Eq. 2 is included. In addition, four mode shapes are included for the simulated defects with d = 15 mm and the corresponding data points are pinpointed on Figure 4 (a) and (c). In a similar way, the ODSs discussed in Figure 3 are marked on Figure 4 (b) and (d) (i.e. 3a, 3d and 3f). For the Al-alloy plate with FBH size 15 mm, an additional measurement is performed up to 300 kHz to validate that all LDR frequencies are indeed below 100 kHz. A difference in LDR behavior is observed between shallow and deep defects. The results are discussed separately for both defect types in the next two sections.

3.1. Shallow defects k < 50 %

The shallow defects (k < 50 %), show a clear local maximum in the DBR curve related to LDR behavior. This strong LDR is illustrated in Figure 4 for a FBH with d = 15 mm (yellow color) and k = 8 %. The LDR is triggered at 20 kHz as proven by the corresponding mode shape (A). From this mode shape, the defect can be easily identified due to the high DBR value of 68 (see Figure 4 (c)). When the relative thickness of the defect increases, the LDR behavior becomes tempered and the related DBR decreases exponentially (see Figure 4 (c,d)). Mode shape (B) corresponds to LDR (at 60 kHz) for the FBH of d = 15 mm (yellow color) and k = 33 %. The defect is still detectable but the decrease in DBR is clear when comparing mode shapes (A) and (B).

For these shallow defects, a good correspondence is found between the LDR frequency deducted from FE simulation (filled symbols) and experiments (open symbols). On Figure 4 (b) and (d), the fundamental LDR frequencies, for which the ODSs were discussed in Figure 3, are indicated. The frequencies match with the numerical predictions and the mode shapes show the strong LDR behavior. Also the analytical estimation (straight line) is in accordance with the results showing the linear dependency of f_{LDR} with k. For defects with small d/t_{defect} ratio, the assumptions of the analytical prediction are not valid resulting in an overestimation of f_{LDR}. This explains the mismatch between the analytical predicted and numerically obtained f_{LDR} for FBH's of diameter d = 10 mm and k > 18 %. To further investigate the validity of Eq. 2, the f_{LDR} results are plotted in function of the defect diameter in Figure 5 for defects of k = 8 % and k = 33 %. Again, a good correspondence is found between the analytical prediction and the FE simulations except for the defects with relative thickness k = 33 % and d < 20 mm. For these defects, the thin plate, clamped boundary assumptions are not valid and the LDR frequency is overestimated. In addition, this figure illustrates the quadratic reduction of f_{LDR} with increasing defect diameter.

In a practical case of NDT using the concept of LDR, the shallow defect's LDR behavior can be detected from the broadband vibration response either manually or automated [21] by exploiting the characteristic high DBR. The size of the defect can be estimated from its ODS at the identified LDR frequency. With known material parameters (i.e. stiffness tensor and density), the defect depth can then be derived using an iterative FE procedure or estimated using an analytical prediction [5].

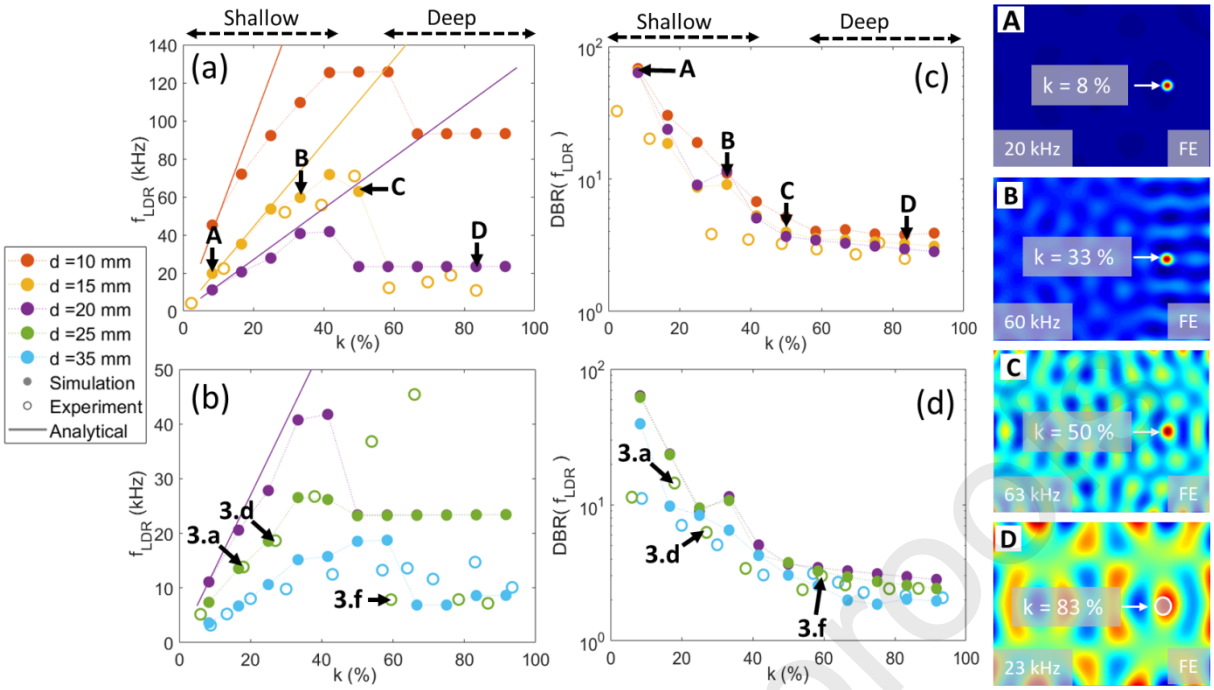

Figure 4: LDR frequency (a,b) and corresponding defect-to-background ratio (c,d) for FBHs in Al-alloy plate. The numerically computed LDR mode shape is provided for the FBHs with d = 15 mm and k = 8, 33, 50 and 83 % (A-D). The markers of the modes shapes shown in Figure 3 are indicated with 3.a, 3.b and 3.c.

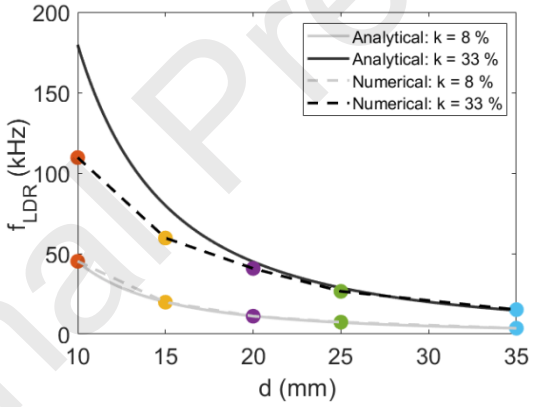

Figure 5: Numerically computed and analytically predicted LDR frequency in function of defect diameter for shallow defects with relative thickness k = 8 and 33 %.

3.2. Deep defects k > 50 %

For the deep defects (k > 50 %), the DBR curve does not show a pronounced maximum (see also inset of Figure 3) that indicates the absence of LDR behavior. This observation is further illustrated by evaluating the mode shapes at maximum DBR for FBHs of d = 15 mm (yellow color Figure 4 (a)) at depth k = 50 and k = 83 % (see Figure 4, mode shapes (C) and (D)). The FBH with k = 50 % shows an increased vibrational amplitude at f_{LDR} = 63 kHz with corresponding DBR = 4. This f_{LDR} is significantly lower than analytically predicted. From observing mode shape (C), the significant vibrational activity of the sound area of the coupon is visible. For the FBH with k = 83 %, the maximum DBR decreases to 3 for the corresponding mode shape (D) at 23 kHz. It is clear that this mode shape is not showing LDR but rather a global plate resonance with an anti-node at the defect's location.

For all simulations, the defects are located at the same position. As a result, in the case of deep defects, it is often the same global resonance that is identified by the maximum DBR. This explains the convergence of f_{LDR} for deep defects to a specific global resonance frequency, for instance 23 kHz in the case of the sample with FBH of diameter 15 and 20 mm (yellow and purple curve in Figure 4 (a)).
A similar observation can be made for the experimental results of deep defects. The frequency of maximum DBR is again related to a global resonance frequency with anti-node at the defect's location. This f_{LDR} thus depends largely on the global plate parameters and only limitedly on the defect parameters. Considering that the global plate dimensions are different in the FE simulation and experiment, it is clear that there is a bad correspondence between f_{LDR} from simulation and experiment.
The limited DBR value makes the detection of these defects by ODS investigation impossible. As such, other methods are needed to detect these deep defects.

4. LDR behavior of FBHs and delaminations in CFRP plate

To verify if the observation made in Section 3 are valid for more complex materials, a similar investigation to the LDR behavior of FBHs is performed for the CFRP material. In composite materials, FBHs are popular for benchmarking NDT method because a FBH mimics a delamination with size and depth controlled through the high speed milling process. In order to validate the similarity in vibrational response between FBHs and delaminations, FE simulations of delaminations are also included and discussed in a separate section. The defects' parameters, namely: type, diameter d and relative thickness k, were listed in Table 2 (FE simulation) and Figure 2 (experiments).

4.1. LDR behavior of FBHs

The results for the FBH defects are shown in Figure 6. For the FBHs, experiments as well as simulations are performed indicated by the empty and filled markers, respectively. As was the case for the FBHs in Al-alloy (see Figure 4), two specific regions can be distinguished.
The first region corresponds to the shallow defects (k < 50 %). The relatively thin FBHs show a clear LDR behavior. The LDR frequency increases linearly with k for defects with relatively low t_{defect}/d ratio, in accordance with the analytical solution [4], and somewhat less than linearly for defects with higher t_{defect}/d ratio (see Figure 6 (a,b)). The FE results match well with the experimental observations. Figure 6 (A), (B) and (C) show the ODS at f_{LDR} for three shallow FBHs of d = 15 mm (purple color). The resonant behavior of the defect is visible in each ODS. The ODSs also illustrate the decrease in DBR with increasing relative thickness (see also DBR values in Figure 6 (c)). As can be seen in Figure 6 (c), the DBR value is lower for the experimental results compared to the simulations. Firstly, there is the effect of damping which is not present in the computed mode shapes. This results in a zone of relatively high amplitude around the excitation location (see ODS (B) and (C)) which decreases the DBR at LDR. Secondly, the ODS at f_{LDR} is influenced by plate resonances at frequencies close to f_{LDR}. This also results in an increase of the amplitude at the sound region and a reduction of DBR. At last, the measurement noise reduces the DBR slightly. The reduction in maximum DBR can further complicate the LDR identification in practical NDT applications.

The second region corresponds to the deep defects (k > 50 %) for which no LDR behavior could be detected. In this case, the maximum in the DBR is low and related to a global resonance of the plate with an anti-node at the location of the defect. In case of the simulation data with fixed defect location, this results in the convergence of f_{LDR} to a specific global resonance. The absence of LDR is further

illustrated using the experimentally measured ODS at maximum DBR (i.e. f = 18 kHz) for the FBH of d = 15 mm and k = 58 % (see Figure 6 (D)). Note that this ODS, by coincidence, shows LDR behavior for the shallow FBH of d = 25 mm and k = 31 %.

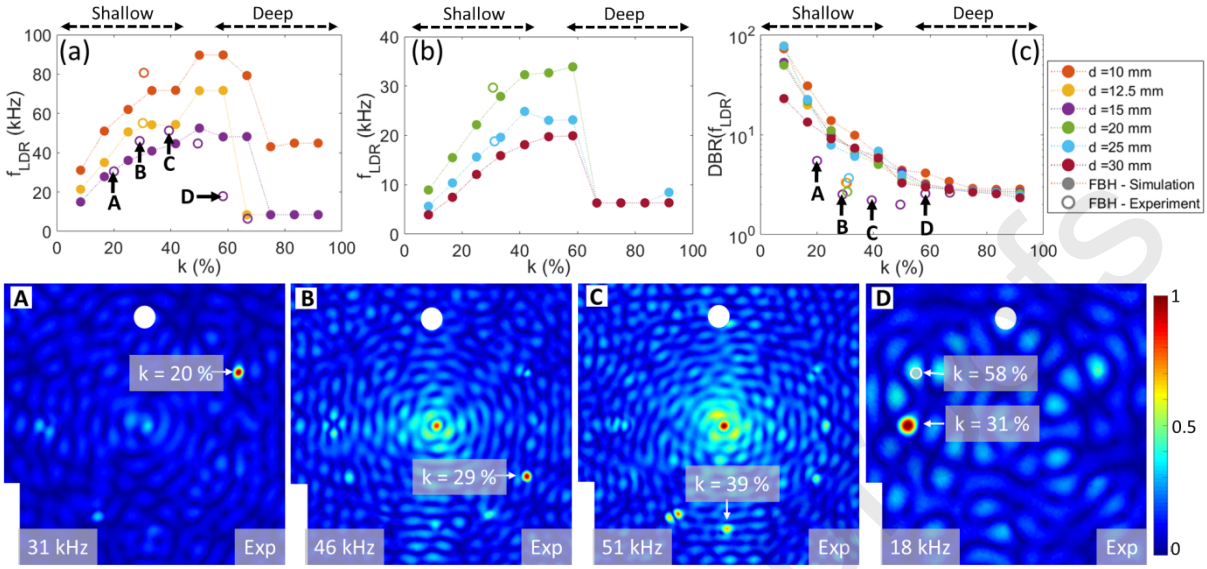

Figure 6: LDR frequency and corresponding defect-to-background ratio (DBR) for FBHs in CFRP plate.
The experimentally observed ODS (after normalization) is provided for FBHs with d = 15 mm and k = 20, 29, 39 and 58 %.

4.2. LDR behavior comparison of FBHs and delaminations

Figure 7 shows the comparison of numerically computed LDR frequency between FBHs and delaminations with diameter 15 mm. Cross sectional views of three mode shapes of each defect type are included. The results for the shallow defects (k < 50 %) indicate the similarity between shallow delaminations and shallow FBHs in both the LDR frequency as well as their mode shape (see Figure 7 (A) and (B)).

In contrast, the correspondence between FBHs and delaminations diminishes for deep defects. For the FBH, the convergence of f_{LDR} to a global resonance frequency is clear (see Figure 7). In the case of a deep delamination, the frequency of maximum *DBR* of the thick top part of the delamination coincides with the f_{LDR} of the corresponding thin bottom part of the delamination at the backside as deducted from delamination mode shape (B) and (C). This phenomenon is caused by the interaction between the two sides of the delamination and results in the symmetry of the f_{LDR} curve around k = 50 %. Only the deepest delamination is an exception to this. It is believed that this reciprocity phenomenon will be more pronounced in a real case as the simulation assumed the absence of interfacial interactions. Because the maximum DBR value is still very low for these deep delaminations, this phenomenon does not help in detecting them.

This comparative study shows that the use of FBHs for detectability evaluation of delaminations by means of LDR is only valid for shallow defects.

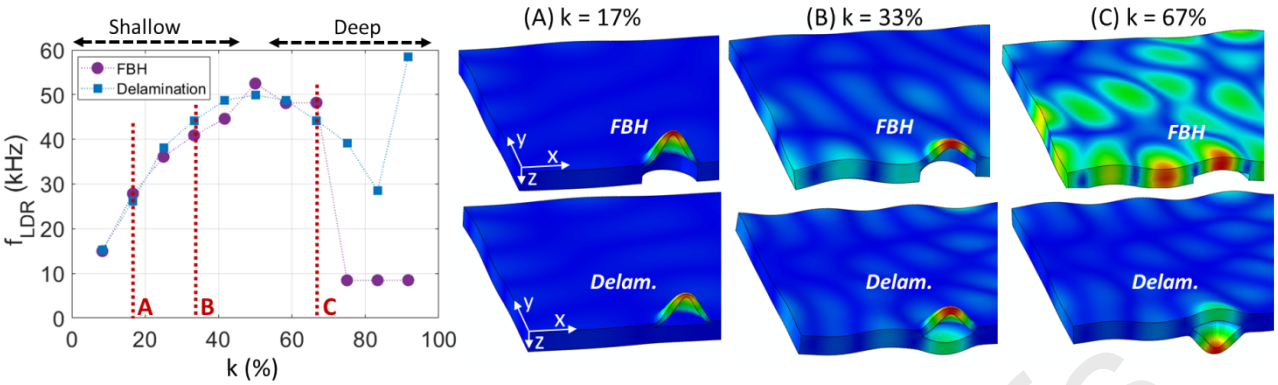

Figure 7: Numerically computed LDR frequency for FBHs and delamination of d = 15 mm in CFRP plate with corresponding profile cuts of six LDR mode shapes.

Looking back to Section 3, it is clear that the LDR behavior of the defects in the CFRP coupon is similar to the LDR behavior of the defects in the Al-alloy coupon. Again, it is concluded that shallow defects show a pronounced LDR behavior which allows for shallow defect detection using LDR identification in the broadband frequency response of the structure. On the contrary, deep defects do not show LDR behavior. An attempt can be made to exploit the non-linear response of deep defects [22-24]. For instance for delaminated sandwich structures, it has been shown that the nonlinear response of a far-sided delamination, i.e. a deep defect, can be detected and reveals the delaminated area [25]. Alternatively, energy based approaches can be used. A promising energy based method will be presented in the next section.

5. Opportunities for deep defect detection – Band power

The parametric evaluation of LDR for FBHs in Al (Section 3) and CFRP (Section 4) revealed that the detection of deep defects by searching for local resonances in ODSs is not possible. Indeed, the phenomenon of local defect resonance does not appear if the stiffness contrast between defect and sound area is not sufficiently high. Nevertheless, deep defects are still related to a small local reduction in bending stiffness which thus should lead to a slightly higher vibrational activity compared to the surrounding sound material. This is also deducted from Figure 3 in which *DBR(f) > 1* for the large majority of frequency bins. In order to make this more visible, these three *DBR(f)* curves are repeated in Figure 8 together with the curves after applying a Savitzky-Golay smoothing filter. The area below the *DBR(f)* curves, for which *DBR(f)* > 1, is shaded as it is a measure for this elevated vibrational activity of the defect compared to the sound material. The elevated activity is very pronounced for shallow damages especially at the LDR modes (see large shaded area for defect k = 18 %). However, also for deeper defects, which do not show LDR behavior, this elevated activity is observed (see shaded area for defect k = 59 %). This characteristic can be exploited for defect detection using a weighted band power (WBP) calculation which is defined as:

$$WBP(x,y,f_1,f_2) = \int_{f_1}^{f_2} \frac{PSD_{V_z}(x,y,f)}{PSD_{U_{ref}}(f)\,.\,WD(r,f)} df$$

$$\text{with} \quad PSD_{V_z}(x,y,f) = \frac{V_z(x,y,f)^2}{f_s} \quad PSD_{U_{ref}}(f) = \frac{U_{ref}(f)^2}{f_s} \tag{3}$$

Where PSD_{V_z} and $PSD_{U_{ref}}$ are the power spectral density of the scan point at location (x,y) for frequency f, of respectively the out-of-plane velocity V_z and excitation voltage U_{ref} signal. $WD(r,f)$ are the frequency specific weighting functions and f_s is the sampling frequency. The frequency limits f_1 and f_2 must lie within the frequency bandwidth of the excitation signal. The weighting functions WD are introduced to compensate for the damping of the elastic waves. For each frequency bin f, this weighting function is obtained by curve fitting a second order exponential decay function to the scatter plot of PSD_{V_z} (evaluated at frequency f) in function of its distance to the excitation position $r = \sqrt{(x-x_{PZT})^2+(y-y_{PZT})^2}$. This procedure is further discussed in Section 5.2. As such, the WBP represents the (weighted) power of vibration over the frequency band of interest.

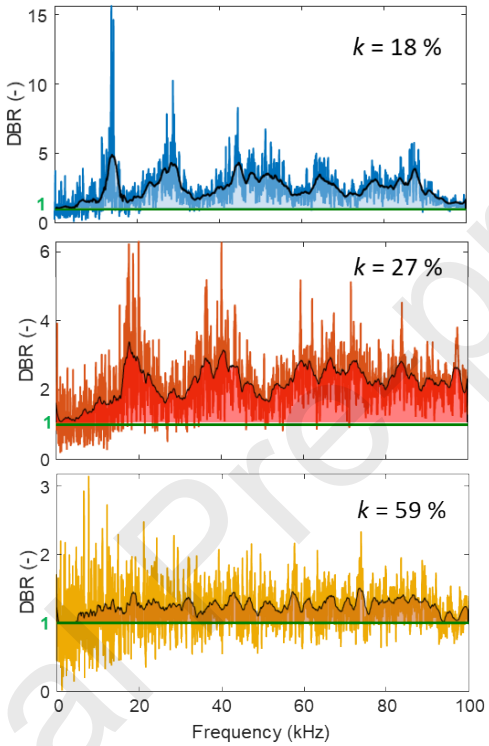

Figure 8: Experimentally obtained defect-to-background ratio (DBR) in function of frequency for three FBHs in the Al-alloy plate (d = 25 mm, k = 18, 27 and 59 %). Indication of area under Savitzky-Golay filtered DBR curve (black line) for which DBR > 1.

5.1. Aluminum alloy

For the three Al-alloy plates (defects with d = 15, 25 and 35 mm), the band power (BP) map is calculated over the total excitation bandwidth (f_1 = 1 kHz, f_2 = 100 kHz) without using weighting functions ($WD(r,f) = 1$). For each plate, the calculation time is around 5s when performed on a Dell Latitude with intel core i7-7820 HQ CPU @2.90 MHz and 32 GB RAM memory. The low material damping of aluminum allows for omitting the weighting function calculation step. The results are normalized and median filtered (with mask [3X3]) to remove erroneous measurement points. Figure 9 presents the obtained band power maps in logarithmic scale.

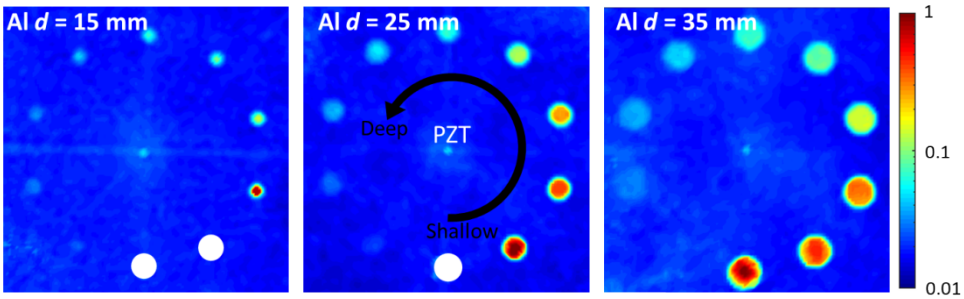

Figure 9: Band power (1 → 100 kHz, *WD* = 1) for Al-alloy plates with FBHs of *d* = 15 mm (a), *d* = 25 mm (b) and *d* = 35 mm (c).

The relative thickness of the FBH determines the local stiffness reduction which in turn determines the increase in vibrational activity. This is seen in Figure 9, where an elevated BP is visible especially for the most shallow defects. Note that the defects increase in relative thickness, starting from the bottom and going in counter-clockwise direction (as indicated in Figure 9(b)). Although the BP decreases for deep defects, all FBHs up to *k* = 90 % are visually distinguishable in the maps. Thus despite the absence of prominent LDR behavior, deep defect can be detected by taking advantage of the small increase in vibrational activity summed over a large amount of frequencies.

In a successive step, these band power images can be used for automated defect identification sizing. As an example, Figure 10 shows the identification and sizing of the FBHs in the Al-alloy plate with FBHs of diameter 25 mm. The black and white image is obtained after thresholding the band power frame with a threshold equal to 0.05. The actual defect size is indicated with red circles. The shallow defects (low *k* value) are overestimated in size whereas the deep defects (high *k*) are underestimated. The deepest FBH is not detected using this 0.05 threshold value. In order to solve this, more advanced adaptive thresholding is required, taking into account the desired probability of detection. If multiple identical samples are available a self-learning approach can be used. However, this is out-of-scope of this study.

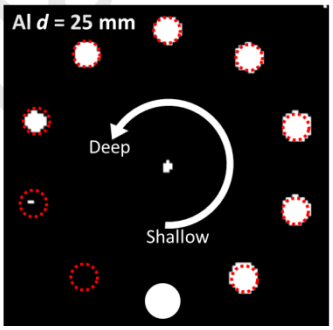

k (%)	d* (mm)
6	30
18	29
27	30
38	28
54	27
59	26
66	21
78	5
87	-

Figure 10: Defect sizing on band power image for Al-alloy with FBHs of diameter 25 mm using 5 % threshold. Actual defect size is indicated with red circles.

5.2. CFRP

The same procedure is performed to calculate the BP map for the CFRP plate (see Figure 11 (a)). An elevated power around the excitation location is observed. This is caused by the relatively high material damping of CFRP compared to Al, the increased maximum frequency (i.e. 150 kHz instead of 100 kHz) and the shorter chirp length (i.e. 20 ms compared to 40 ms). This increase in BP around the excitation

location partially obscures the effect of the defects. This is especially the case if defects would be located close to the PZT excitation source.

In order to compensate for the damping, the frequency specific weighting functions $WD(r,f)$ are determined. Figure 11 (b) illustrates the scatter plot of PSD_{V_z} and second order exponential decay fit curve for the ODS at f = 65 kHz. This frequency-specific damping compensation is required due to the strong frequency dependence of elastic wave damping in CFRPs. The weighting method further assumes directional independent damping which is valid for this quasi-isotropic CFRP coupon, though it can be easily extended to account for directional damping features.

The final resulting WBP is shown in Figure 11 (c). The use of the weighting function and the associated curve fitting procedure increases the calculation time to around 1 minute. Further reduction of the calculation time is possible by parallelization of the procedure. The improvement of using the weighting filter leads to a visible impression of all defects, including those for which no LDR behavior could be detected. Apart from the increased vibrational response at the defects and the effect of damping, other elastic wave artifacts are captured in the WBP map. The diagonals show an increased WBP due to the local constructive interference of travelling elastic waves reflected from the plate's boundaries. Also around the FBHs, the WBP is influenced due to wave reflection, attenuation and interference effects.

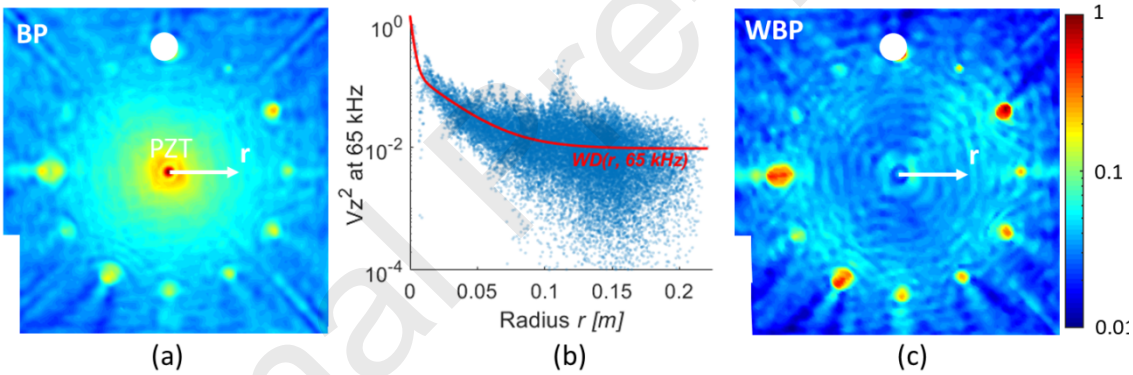

Figure 11: (a) Band power map (1 → 150 kHz), (b) Nodal PSD_{V_z} in function of distance to excitation location (i.e. radius r) for ODS at 65 kHz and (c) Weighted band power (1 → 150 kHz) for CFRP plate with FBHs.

6. Conclusions

The out-of-plane local defect resonance (LDR) behavior of flat bottom holes (FBHs) is parametrically evaluated for Al-alloy and CFRP material. Finite element modal analysis as well as experiments using contact excitation and scanning laser Doppler vibrometry are performed. For each FBH of specific diameter and thickness, the defect-to-background ratio (DBR) is calculated for all modes shapes (FE simulation) and operational deflection shapes (experiment). Local maxima in the DBR curves are determined and investigated for LDR behavior.

For the shallow defects, i.e. FBHs with relative thickness smaller than 50 %, clear LDR behavior at a frequency proportional to the ratio of defect thickness over squared diameter is detected. A good correspondence between experiments and simulations is found. Additionally, it is shown that a shallow FBH is representative for a shallow delamination in layered composite materials when investigating the LDR behavior. It is concluded that such shallow defects can be detected by searching for LDR behavior in the broadband frequency response of the test specimen.

For the deep defects, i.e. relative thickness higher than 50 %, no LDR behavior corresponding to a high DBR is present. As a result, using the classical LDR identification techniques for detection of deep defects is impossible.

While the limited local stiffness reduction of deep defects does not result in LDR, it does slightly increase the vibrational activity of the defected area. This observation is exploited using a weighted band power calculation in which the small increase in local vibrational activity is summed over a large amount of excitation frequencies. Based on the experiments, it is shown that this simple approach allows for the detection of deep defects up to 90 % of the test specimen's depth.

Acknowledgments

Joost Segers is a PhD fellow of the Research Foundation-Flanders (FWO, Grant no. 1148018N). The authors further acknowledge FWO (Grant no. 12T5418N) and the SBO project DETECT-IV (Grant no. 160455), which fits in the SIM research program MacroModelMat (M3) coordinated by Siemens (Siemens PLM software, Belgium) and funded by SIM (Strategic Initiative Materials in Flanders) and VLAIO (Flemish government agency Flanders Innovation & Entrepreneurship).

References

1. Tenek, L.H., E.G. Henneke, and M.D. Gunzburger, *Vibration of delaminated composite plates and some applications to non-destructive testing.* Composite Structures, 1993. **23**: p. 253-262.
2. Solodov, I., et al., *A local defect resonance to enhance acoustic wave-defect interaction in ultrasonic nondestructive evaluation.* Applied Physics Letters, 2011. **99**(21).
3. Segers, J., et al., *Towards in-plane local defect resonance for non-destructive testing of polymers and composites.* NDT & E International, 2018. **98**: p. 130-133.
4. Solodov, I., J. Bai, and G. Busse, *Resonant ultrasound spectroscopy of defects: Case study of flat-bottomed holes.* Journal of Applied Physics, 2013. **113**(22).
5. Solodov, I., M. Rahammer, and M. Kreutzbruck, *Analytical evaluation of resonance frequencies for planar defects: Effect of a defect shape.* NDT & E International, 2019. **102**: p. 274-280.
6. Solodov, I., D. Derusova, and M. Rahammer, *Thermosonic Chladni figures for defect-selective imaging.* Ultrasonics, 2015. **60**: p. 1-5.
7. Kolappan Geetha, G. and D. Roy Mahapatra, *Modeling and simulation of vibro-thermography including nonlinear contact dynamics of ultrasonic actuator.* Ultrasonics, 2019. **93**: p. 81-92.
8. Roy, S., T. Bose, and K. Debnath, *Detection of local defect resonance frequencies using bicoherence analysis.* Journal of Sound and Vibration, 2019. **443**: p. 703-716.
9. Hettler, J., et al., *Detection and Characterization of Local Defect Resonances Arising from Delaminations and Flat Bottom Holes.* Journal of Nondestructive Evaluation, 2017. **36**(1).
10. Segers, J., et al., *Investigation to Local Defect Resonance for Non-Destructive Testing of Composites.* The Eighteenth International Conference of Experimental Mechanics, 2018. **2**(8).
11. Solodov, I. and M. Kreutzbruck, *Single-sided access remote imaging via resonant airborne activation of damage.* NDT & E International, 2019. **107**.
12. Solodov, I., A. Dillenz, and M. Kreutzbruck, *A new mode of acoustic NDT via resonant air-coupled emission.* Journal of Applied Physics, 2017. **121**(24).
13. Sarens, B., et al., *Investigation of Contact Acoustic Nonlinearity in Delaminations by Shearographic Imaging, Laser Doppler Vibrometric Scanning and Finite Difference Modeling.* IEEE Transactions on Ultrasonics, 2010. **57**(6): p. 1383-1395.

14. Lamboul, B. and D. Osmont, *Delamination detection in foam core composite structures using transient flexural wavefields.* Journal of Sound and Vibration, 2016. **366**: p. 190-198.
15. Dionysopoulos, D., et al., *Imaging of barely visible impact damage on a composite panel using nonlinear wave modulation thermography.* NDT & E International, 2018. **95**: p. 9-16.
16. Klepka, A., et al., *Impact damage detection in laminated composites by non-linear vibro-acoustic wave modulations.* Composites Part B: Engineering, 2014. **65**: p. 99-108.
17. Derusova, D., et al., *Ultrasonic spectroscopic analysis of impact damage in composites by using laser vibrometry.* Composite Structures, 2019. **211**: p. 221-228.
18. Girolamo, D., H.Y. Chang, and F.G. Yuan, *Impact damage visualization in a honeycomb composite panel through laser inspection using zero-lag cross-correlation imaging condition.* Ultrasonics, 2018. **87**: p. 152-165.
19. Stockist, A.-F.a.N.-F.M. *Aluminium Alloys - Aluminium 6082 Properties, Fabrication and Applications*. 2005; Available from: https://www.azom.com/article.aspx?ArticleID=2813.
20. Martens, A., et al., *Characterization of the orthotropic viscoelastic tensor of composites using the Ultrasonic Polar Scan.* Composite Structures, 2019. **230**.
21. Segers, J., et al., *Efficient automated extraction of local defect resonance parameters in fiber reinforced polymers using data compression and iterative amplitude thresholding.* Journal of Sound and Vibration, 2019. **463**.
22. Fierro, G.P.M. and M. Meo, *A combined linear and nonlinear ultrasound time-domain approach for impact damage detection in composite structures using a constructive nonlinear array technique.* Ultrasonics, 2018. **93**: p. 43-62.
23. Solodov, I., N. Krohn, and G. Busse, *CAN: an example of nonclassical acoustic nonlinearity in solids.* Ultrasonics, 2002. **40**(1): p. 621–625.
24. Fierro, G.P.M. and M. Meo, *Nonlinear elastic imaging of barely visible impact damage in composite structures using a constructive nonlinear array sweep technique.* Ultrasonics, 2018. **90**: p. 125-143.
25. Zhang, S., et al., *Far-sided defect recognition of FRP sandwich structures based on local defect resonance*. Journal of Sandwich Structures & Materials, 2019(April): p. 1-12.

Highlights

- Shallow defects show clear out-of-plane local defect resonance behavior.
- Deep defects do not show pronounced out-of-plane local defect resonance behavior.
- Detection of defect by searching for LDR behavior in operational deflection shapes is only possible for shallow defect.
- Weighted band power calculation significantly improves the detectability of deep defects compared to LDR.

Declaration of interests

☒ The authors declare that they have no known competing financial interests or personal relationships that could have appeared to influence the work reported in this paper.

☐The authors declare the following financial interests/personal relationships which may be considered as potential competing interests: